

Magnetic origin of the discrepancy between stellar limb-darkening models and observations

Received: 23 May 2023

Accepted: 14 March 2024

Published online: 12 April 2024

 Check for updates

Nadiia M. Kostogryz¹✉, Alexander I. Shapiro¹, Veronika Witzke¹, Robert H. Cameron¹, Laurent Gizon^{1,2}, Natalie A. Krivova¹, Hans-G. Ludwig³, Pierre F. L. Maxted⁴, Sara Seager^{5,6,7}, Sami K. Solanki¹ & Jeff Valenti⁸

Stars appear darker at their limbs than at their disk centres because at the limb we are viewing the higher and cooler layers of stellar photospheres. Yet, limb darkening derived from state-of-the-art stellar atmosphere models systematically fails to reproduce recent transiting exoplanet light curves from the Kepler, TESS and JWST telescopes—stellar brightness obtained from measurements drops less steeply towards the limb than predicted by models. Previous models assumed stellar atmospheres devoid of magnetic fields. Here we use stellar atmosphere models computed with the three-dimensional radiative magnetohydrodynamic code MURaM to show that a small-scale concentration of magnetic fields on the stellar surface affects limb darkening at a level that allows us to explain the observations. Our findings provide a way forward to improve the determination of exoplanet radii and especially the transmission spectroscopy analysis for transiting planets, which relies on a very accurate description of stellar limb darkening from the visible to the infrared. Furthermore, our findings imply that limb darkening allows estimates of the small-scale magnetic field strength on stars with transiting planets.

Efforts to compute stellar limb darkening go back over a century to the classical work of Schwarzschild¹ and Milne². The knowledge of limb darkening is required for numerous astrophysical applications, for example, measurements of stellar diameters with interferometry³, the interpretation of light curves of eclipsing binary stars⁴ and spotted stars⁵, and the interpretation of the centre-to-limb effects observed in local helioseismology^{6,7}.

An iconic modern-day application of limb darkening is for transit light-curve fitting to derive planetary radii with transit photometry

and atmospheric composition with transmission spectroscopy^{8–10}. It relies on the description of stellar limb darkening, which alters the transit profile and depth. Yet there is a conundrum: stellar atmosphere models indicate a substantially stronger drop of the brightness towards the stellar limb than multiple sensitive observations show. This point is made clear by analyses of Kepler and Transiting Exoplanet Survey Satellite (TESS) transit light curves^{11,12}. Further observations include that of α Centauri¹³ with the Very Large Telescope Interferometer (VLTI) and, most recently, that of WASP-39¹⁴ with the James Webb Space

¹Max-Planck-Institut für Sonnensystemforschung, Göttingen, Germany. ²Institut für Astrophysik und Geophysik, Georg-August-Universität Göttingen, Göttingen, Germany. ³Zentrum für Astronomie, Landessternwarte, Heidelberg University, Heidelberg, Germany. ⁴Astrophysics Group, Keele University, Keele, UK. ⁵Department of Physics and Kavli Institute for Astrophysics and Space Research, Massachusetts Institute of Technology, Cambridge, MA, USA. ⁶Department of Earth, Atmospheric and Planetary Sciences, Massachusetts Institute of Technology, Cambridge, MA, USA. ⁷Department of Aeronautics and Astronautics, Massachusetts Institute of Technology, Cambridge, MA, USA. ⁸Space Telescope Science Institute, Baltimore, MD, USA.

✉e-mail: kostogryz@mps.mpg.de

Telescope (JWST.) In particular, ref. 12 compared observed and modelled limb darkening in 33 Kepler and 10 TESS stars with transiting exoplanets. It was found that although all theoretically computed limb darkening, including those based on MPS-ATLAS¹⁵, ATLAS^{16–18}, PHOENIX¹⁹, STAGGER¹¹ and MARCS²⁰ model atmospheres, are in relatively good agreement with each other, they all indicate a steeper drop of the stellar brightness from the centre of a stellar disk towards its limb than observations.

One response to this mismatch has been to include empirical limb-darkening coefficients for each wavelength bin as free parameters when fitting transit light curves²¹. However, increasing the number of free parameters introduces biases and additional uncertainties in the determination of the planetary radius^{21–24}. The problem has been raised to a new level with the advent of the JWST²⁵. The extreme precision transmission spectroscopy data obtained by this telescope require a more accurate transit analysis, which in turn calls for improved theoretical modelling of limb darkening. Similar precision is also anticipated from the Atmospheric Remote-sensing Infrared Exoplanet Large-survey (ARIEL)²⁶ (launch expected in 2029).

Here we show that stellar surface magnetic fields measurably affect limb darkening. The magnetic effect is bound to manifest itself in the available observations as all stars on the lower main sequence are intrinsically magnetic²⁷. Some of these magnetic fields are generated deep within the stellar convective zone by the action of a global stellar dynamo²⁸. Another important component of the stellar surface magnetic field results from the action of a near-surface small-scale turbulent dynamo (SSD)²⁹. Such an SSD fills nearly the entire stellar surface with considerable magnetic flux, thus producing a minimum level of magnetic activity^{30–33}. The turbulent magnetic fields produced by the SSD are always present at the stellar surface independently of the action of the global stellar dynamo and they also modify the stellar photospheric structure^{32,33} (relative to the hypothetical non-magnetic case). Large concentrations of surface magnetic field, resulting from the action of the global dynamo, form active regions (containing, for example, dark spots). While spots produce an offset of the transit curve³⁴, the effect from the spots is not visible on stellar limb darkening unless the planet crosses them during the transit. Smaller concentrations of field resulting from both global and small-scale dynamos lead to the formation of a more homogeneous magnetic network present all over the star, so that a transiting planet always crosses it. In the present study, we show that the mismatch between simulations and Kepler³⁵ measurements disappear after accounting for the effect of the magnetic network on the limb darkening.

Results

The noted discrepancy between high-precision observations and models is showcased in Fig. 1 by a comparison of the observations (where we refer to the average over the Kepler sample) with the reference grid of non-magnetic limb darkening, which shows an offset. To quantitatively describe the offset, we compute the observations–model differences in limb-darkening coefficients used to parameterize limb darkening¹². One, h'_1 , effectively describing the drop in star brightness from disk centre to about 0.75 of the stellar radius (corresponding to $\mu = 2/3$, where μ is a cosine of the heliocentric angle, which is an angle between the line of sight and the normal to the local surface), another, h'_2 , the drop from 0.75 to 0.95 ($\mu = 1/3$) of the stellar radius (see top-right corner in Fig. 1). Observations from Kepler are averaged over tens of stars to increase the signal-to-noise ratio. The model values are taken from the one-dimensional (1D) MPS-ATLAS spectral library^{15,36} (namely, SET 1 from this library, hereafter referred to as REFLD). By computing the observations–REFLD differences, we quantify the limb-darkening conundrum, which we solve by adding the effect of magnetic field.

The primary finding of this study is that the offset between models and observations can be explained by a stellar surface magnetic field. To demonstrate this, we simulated limb darkening as it would

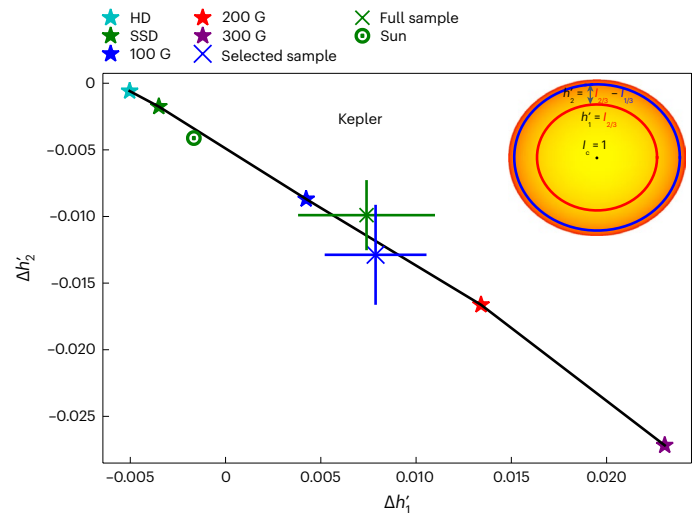


Fig. 1 | Limb darkening in the Kepler passband. The x and y axes express the difference in the limb-darkening coefficients (h'_1 and h'_2) between two sources: one source is always the models without magnetic fields (REFLD) and the other can be models with either fields or observations. The points marked by a cross correspond to the data averaged over the full sample of Kepler stars (green) and over a selected sample including the stars with metallicities $-0.1 < M/H < 0.1$ and transits with an impact factor less than 0.5 (blue). The error bars represent s.e.m. These points show the mean offset between measurements¹² and REFLD¹⁵. The star symbols are our calculations based on MURaM simulations (that is, offsets between our calculations and REFLD) for different magnetization levels (see legend; HD, SSD, 100 G, 200 G, 300 G) in the Kepler passband. The sketch in the right upper corner illustrates the definition of the limb darkening coefficients, where I_c represents the intensity at the disk center, $I_{2/3}$ represents the intensity at $\mu = 2/3$ and $I_{1/3}$ represents the intensity at $\mu = 1/3$. All intensities are normalized to the intensity at the disk center. The solar symbol (Sun) is the measured solar limb darkening in the Kepler passband¹⁵. Our stellar atmosphere models, which include magnetic fields, match both the solar and the stellar observations and provide an explanation for the offsets between Kepler limb darkening relative to models without magnetic field.

be observed for a hypothetical individual star with different levels of magnetization. We find that a star with magnetic fields of about 100 G has the same offset with respect to non-magnetic models as the averaged Kepler observations (Fig. 1). This means that by applying 100 G magnetic field to simulations, we can reconcile them with the observations. This field of about 100 G then corresponds to the averaged magnetization of stars in the Kepler sample.

Our second major finding is that individual stars with the same fundamental parameters (that is, effective temperature, metallicity and surface gravity) will have different limb darkening depending on their magnetization (Fig. 1). This is in stark contrast to what was assumed before. Specifically, we find a clear trend that stars with higher magnetic fields are less dark towards the limb than stars with lower magnetic fields. This is a measurable effect with current high-precision data (see ‘Discussion’). Thus, the measurement of limb darkening opens a new way to measure star surface magnetic fields.

Our modelling approach combines the strengths of 1D and three-dimensional (3D) approaches to stellar atmospheric modelling because each one has its own benefits needed to compute limb darkening. We first use the REFLD grid based on 1D models of stellar atmospheres to get limb darkening on stellar fundamental parameters. Then we use 3D models computed with the radiative magnetohydrodynamic (MHD) code MURaM³⁷ to account for the effect of magnetic field (and realistic treatment of convection). The 1D models are imperative because limb darkening has a strong dependence on stellar fundamental parameters^{15,17}, and the 1D models are computationally cheap enough to be generated on a very fine grid of these parameters. In the

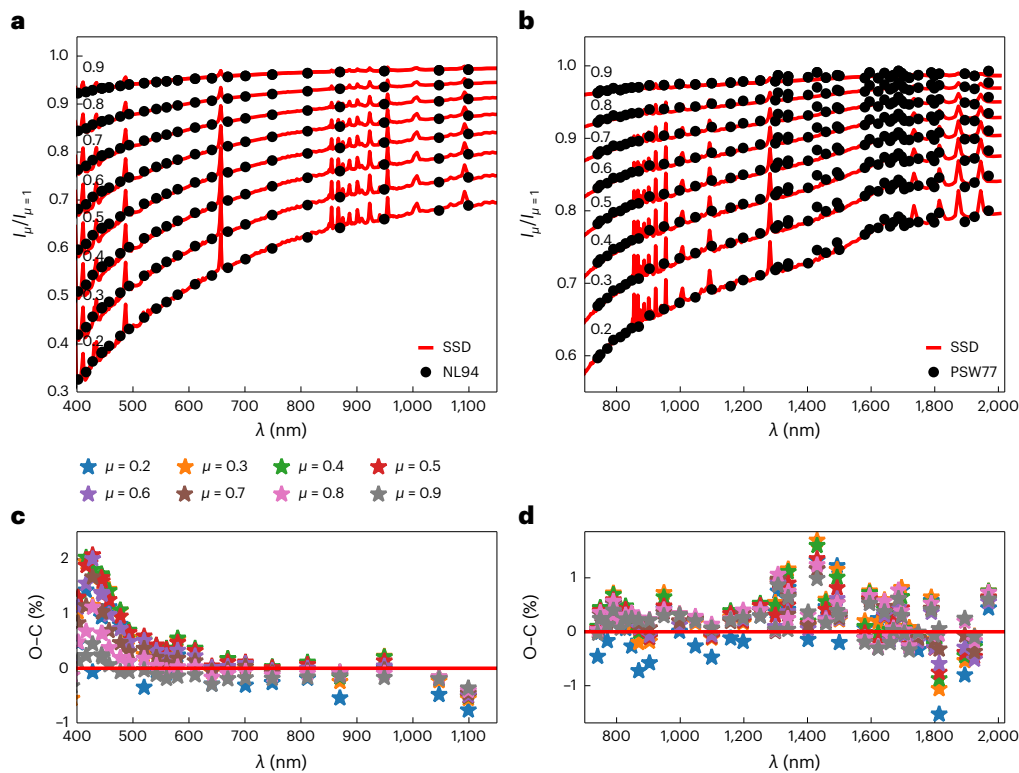


Fig. 2 | Solar limb darkening. **a, b**, The spectral intensities (I_μ) at different disk positions given by μ (labelled on the left side in the figure) normalized to the disk centre intensity ($I_{\mu=1}$). The solid lines correspond to our calculations for the SSD case (that is, they indicate spectra emerging from MURaM cubes as computed with the MPS-ATLAS code) and dot symbols are solar measurements by Neckel and Labs 1994 (NL94)⁴³ (**a**) and Pierce, Slaughter and Weinberger 1977 (PSW77)⁴²

(**b**), where manifestations of solar magnetic activity are excluded to the extent possible. **c, d**, The residuals (stars) in percentage between observations (NL94 in panel **c** and PSW77 in panel **d**) and computations (O–C) at different disk positions (different colours labelled in **c**). The red horizontal lines on these panels point to zero difference between observations and computations. Our model allows us to accurately reproduce solar limb-darkening measurements.

present study, we used the REFLD grid for stars with specific fundamental parameters from the considered Kepler sample. One drawback of the 1D approach is that it relies on the parameterized treatment of convection with the mixing length approximation³⁸ and is intrinsically incapable of accounting for the magnetic field.

To account for the magnetic field, we use 3D MHD models because they allow realistic simulations of near-surface magnetoconvection. The 3D models are too computationally expensive to be produced on a grid of fundamental parameters sufficiently fine to allow reliable interpolations to stars of interest or for each of the stars individually. At the same time, our analysis of recent MURaM simulations^{32,33,39} of magnetized atmospheres of stars with different fundamental parameters shows that the magnetic effect only weakly depends on stellar fundamental parameters and, thus, can be calculated on a rather coarse grid. Moreover, the stars in the considered Kepler sample have near-solar fundamental parameters, so for the purposes of the present study we restrict MURaM simulations (and their post-processing) to the solar atmosphere. In a forthcoming publication, we will extend our investigation to a broader sample of stars.

Our calculations of the magnetic effect on limb darkening are performed in two steps. In the first step, we simulate the magnetized stellar atmosphere with the MURaM code. MURaM is capable of self-consistently simulating the contribution from the action of an SSD^{29,32,33,40}. The effect of magnetic fields brought about by the global dynamo is simulated by adding homogeneous vertical magnetic fields of 100 G, 200 G and 300 G to the initial SSD set-up⁴¹ (hereafter referred to as 100 G, 200 G and 300 G cases, respectively). These initially homogeneous and vertical magnetic fields rapidly evolve to a statistically steady state as our simulations relax. This state is highly

inhomogeneous: strong, nearly vertical magnetic fields condense in the downflow lanes (intergranular lanes), while convective cells (granules) harbour relatively weak fields (Methods and Extended Data Fig. 1).

In the second step, we bridge atmospheric models produced by MURaM to observational data. We make the connection by ‘post-processing’ the MURaM output, by ray tracing through the cubes (representing stellar atmosphere) along several directions (Methods). Along each ray, we compute the intensity emerging from the cube by using the MPS-ATLAS code, which uses the temperature and pressure along the ray. We integrate over all rays emerging from the cube along the given direction.

Magnetic limb darkening in Kepler measurements

We now turn to a more detailed description of the results in context with the physics. Our calculations indicate that spatially resolved measurements of the quiet Sun’s limb darkening^{42,43} can be very accurately reproduced by the SSD simulations that account for the intrinsic magnetization of the quiet Sun (Figs. 1 and 2). The inclusion of an additional magnetic field representing the global dynamo does not match the solar observations as the simulation systematically shows larger residuals to solar observations compared with the SSD simulations (Methods and Extended Data Fig. 2). This is reassuring, as the spatially resolved solar limb-darkening observations have been processed to avoid any distortion by magnetic activity⁴³ and, thus, should correspond to the minimum possible magnetic activity, which is produced by the SSD set-up (see Methods for more details).

In contrast to the solar case, the explanation of the Kepler measurements requires the action of the global dynamo. Indeed, the point representing the mean offset for our sample of 30 Kepler stars

Table 1 | Limb-darkening coefficients in the Kepler passband for the Sun

Coefficients	Passband	REFLD	HD	SSD	100 G	200 G	300 G
h'_1	Kepler	0.8346	0.8296	0.8311	0.8388	0.8480	0.8576
h'_2	Kepler	0.2074	0.2068	0.2057	0.1987	0.1908	0.1802

(hereafter, full sample; Methods) lies very close to the lines connecting the points that illustrate different magnetic cases and next to the calculations corresponding to the 100 G case (Fig. 1). At the same time, the offsets of individual stars in the full sample show notable scatter (Extended Data Fig. 3a), which averages out when the mean offset is calculated. In addition to the full sample, we also consider a selected sample of 8 Kepler stars with $-0.1 \leq M/H \leq 0.1$ (so that they are better described by our solar simulations) and impact parameters of the transit $b < 0.5$ (reducing the errors in the limb-darkening extraction). The mean offset for the selected sample is very close to the mean offset of the full sample but the individual stars show much less scatter around the simulations (Extended Data Fig. 3b).

The close alignment of the mean offsets with the simulation line implies that our calculations with magnetic fields allow us to simultaneously explain the mean offsets in both limb-darkening coefficients and, therefore, reproduce the observed limb darkening within the error bars. Clearly, the magnetic field removes the discrepancy in the limb darkening, and its neglect in earlier models is probably the cause of this discrepancy. We note that our result does not necessarily imply that stars in the Kepler samples are on average more active than the Sun. Stellar measurements correspond to limb darkening along the transit path without any option of removing contributions from magnetic activity. Thus, the limb darkening obtained from planetary transits of stars will inherently contain contributions of magnetic activity. Consequently, a stronger magnetic field is needed to reconcile stellar models and observations.

All in all, our calculations show that magnetic fields make the stellar limb darkening less steep, leading to an increase (compared with the non-magnetic limb darkening) of the brightness at 0.75 of the stellar radius ($\mu = 2/3$) and to an even stronger increase at 0.95 of the stellar radius ($\mu = 1/3$). The smallest offset relative to the non-magnetic case is caused by the magnetic fields generated by an SSD (green star in Fig. 1). Despite the fact that an SSD fills the entire solar photosphere with a relatively large magnetic field (for example, the mean vertical field, $\langle |B_z| \rangle$, at the visible surface is about 70 G; (ref. 33)), only a small fraction of these fields condense to local concentrations harbouring strong, that is, kilogauss magnetic fields^{32,33,40} resulting in only moderate heating of the photosphere.

In contrast, to the magnetic fields generated by an SSD, the fields brought about by the global dynamo, for example, those forming plages and the magnetic network of the Sun, have a more inhomogeneous spatial distribution and cluster in concentrations of up to several kilogauss^{44,45}. These concentrations are often described as magnetic flux tubes⁴⁶ and produce substantial changes in the thermal structure of the photosphere. Consequently, even a spatially averaged field of 100 G (once it has formed kilogauss concentrations through its interaction with the convection) in addition to the SSD-generated field produces a much stronger change of limb darkening than the pure SSD case. Larger spatially averaged magnetic flux densities, for example, 200 G and 300 G added to SSD simulations, lead to correspondingly larger changes of the limb darkening (Fig. 1).

In Table 1, we present the values of h'_1 and h'_2 coefficients for REFLD and 3D MHD MURaM simulations in the Kepler passband. One can see that limb darkening from REFLD and HD MURaM simulations (i.e. without magnetic field) are not identical (so that the cyan star symbol in Fig. 1 is not exactly at the origin). This is because REFLD are based on 1D calculations where convection is parameterized following the mixing length approximation³⁸ while MURaM performs realistic 3D

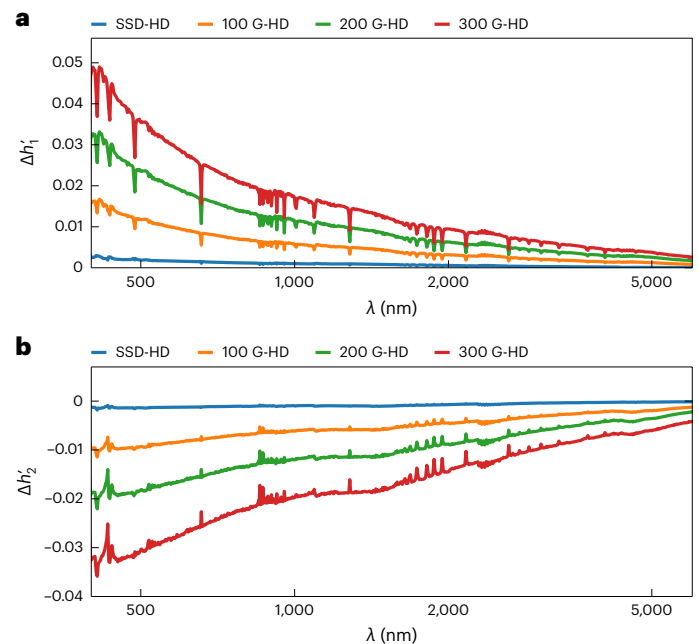


Fig. 3 | Wavelength-dependent limb-darkening coefficients. a, b, We show the differences between limb darkening coefficients ($\Delta h'_1$ in a and $\Delta h'_2$ in b) resulting from MHD simulations with magnetic fields (SSD, 100 G, 200 G, 300 G) and from non-magnetic (HD) simulations. The colours distinguish between the various magnetic (SSD, 100 G, 200 G, 300 G) simulations entering the difference (see legend). The spectral resolving power of the calculations is about 400. The effect of the magnetic field on the limb darkening persists from the ultraviolet to the visible and into the infrared spectral domains.

simulations of convection. We note that despite this imperfection in treatment of the convection, 1D models allow reliable calculations of the non-magnetic limb darkening and their dependencies on stellar fundamental parameters when the mixing length and overshoot parameters are adequately chosen^{17,36}.

Magnetic limb darkening in the JWST era

The effect of the magnetic field on limb darkening affects the interpretation of the JWST transmission spectroscopy data. Indeed, the first JWST observations of transits in the WASP-39 b system¹⁴ performed with the NIRSpec⁴⁷ PRISM showed that the deviation between observations and the currently available models persists throughout the spectral domain of these observations (about 0.5–5.5 μm). To quantify the effect of magnetic field on limb darkening over the JWST spectral domain, we show the dependence of $\Delta h'_1$ and $\Delta h'_2$ on the average magnetic field (with respect to the field-free MURaM HD simulation) as a function of wavelength in Fig. 3. The amplitude of the magnetic effect decreases towards longer wavelengths where emergent intensity is less sensitive to temperature changes caused by the magnetic field. At the same time $\Delta h'_1$ and $\Delta h'_2$ have rather complex spectral profiles, especially in the visible spectral domain where the darkening of the limb is strongly affected by atomic and molecular lines.

The magnetically induced change of the limb darkening modifies the entire shape of transit profiles (Extended Data Fig. 4) and, in particular, the transit depth, which plays a crucial role in determining the radius of a transiting planet. The effect is especially strong

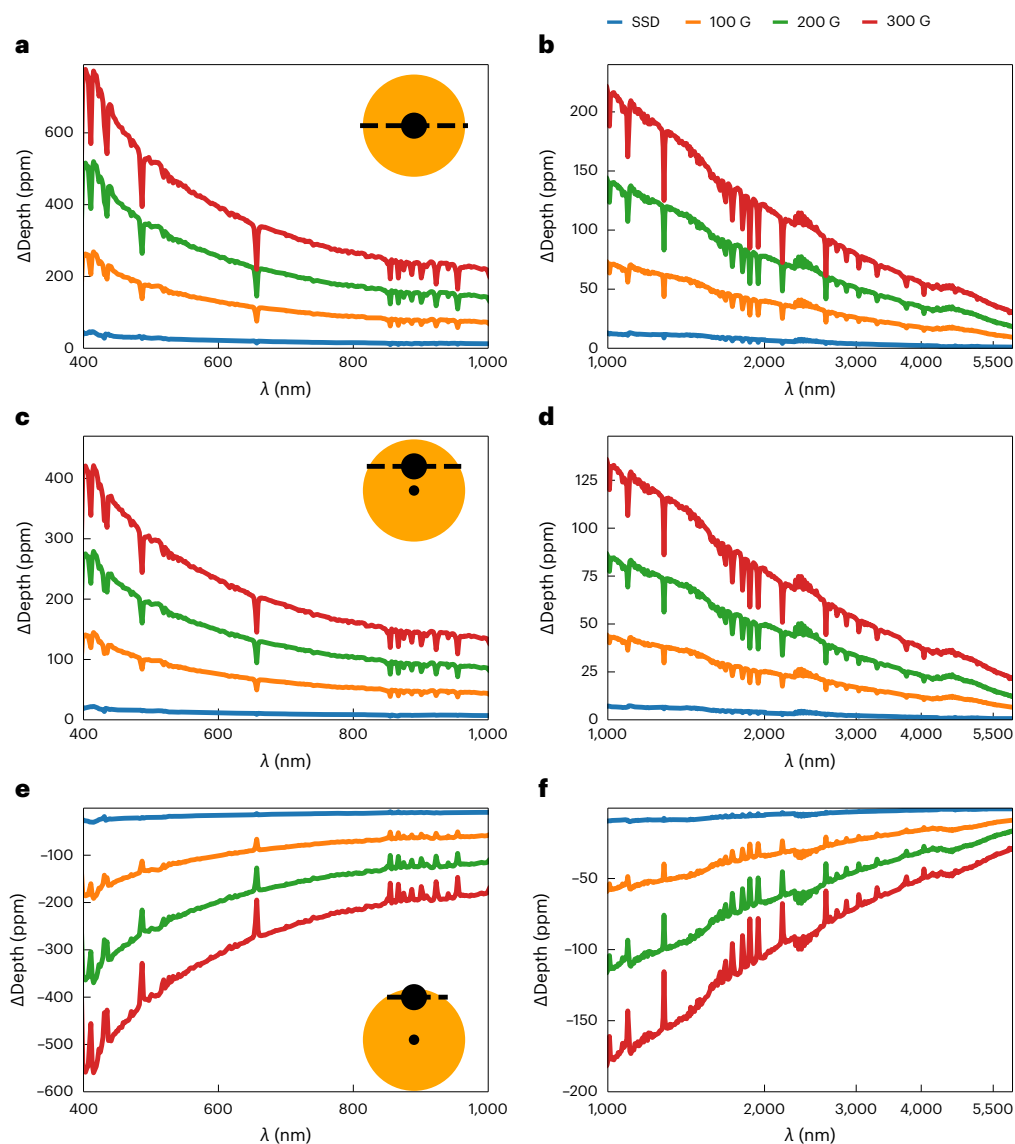


Fig. 4 | Effect of surface magnetic field on transit depth for the exemplary case of a Jupiter-size planet transiting a solar twin. a–f, The difference in the depth of the transit (ΔDepth) calculated with the darkening of the limb corresponding to different degrees of magnetization (different colours) with respect to the darkening of the non-magnetic limb (HD) in ppm. The two columns show the ΔDepth at wavelengths shorter than (a, c, e) and longer than

(b, d, f) 1,000 nm. The three rows correspond to different impact parameters ($b = 0.0$ (a, b), $b = 0.5$ (c, d) and $b = 0.9$ (e, f)) describing the transit path, which is schematically shown in the top-right corner of a, c and e. The bigger circle represents the star and the smaller represents the planet. In general, the difference in transit depth is always larger for stronger average stellar fields and is largest in the ultraviolet while decreasing towards longer wavelengths.

shortwards of 2,000 nm, for example, a magnetic field of 100 G would induce a change of the transit depth larger than about 30–40 ppm for a Jupiter-size planet transiting the Sun (Fig. 4). Such changes can be observed with JWST even for a single transit observation and will also interfere with the interpretation of the JWST transit light curves. Indeed, the first JWST results¹⁴ indicate that the transit curves are not contaminated by systematic effects in most spectral channels, and the noise can be reduced to just a couple of ppm per spectral bin for most of the exoplanet target stars JWST observes (see Fig. 8 in ref. 14). Further observations also indicate that the precision of JWST transit depth measurements reaches the level given by the photon noise, which ranges from several up to hundred ppm depending on the brightness of a star, spectral resolution and wavelength domain of the observations^{48–51}.

We expect the magnetic effect to also be measurable with the forthcoming PLATO mission. Indeed, our calculations for a central transit and a planet-to-star radii ratio of 0.1 show that the effect of a

100 G magnetic field on transit depth is 116 ppm. Corresponding values for 200 G and 300 G are 261 ppm and 405 ppm, respectively. This is substantially higher than the expected PLATO precision (50 ppm for $V = 11$ mag).

Discussion

Small-scale surface magnetic fields previously ignored in modelling of stellar limb darkening modify the atmospheric structure and therefore stellar limb darkening. We have shown that adding such magnetic fields into 3D radiation MHD simulations of stellar atmospheres solves the limb-darkening conundrum, that is, the inability of 1D and 3D magnetic field-free models of stellar atmospheres to return limb-darkening profiles consistent with observations.

The dependence of the limb darkening on the surface magnetic field can be seen as a curse or a blessing depending on one's point of view. On the one hand, it introduces one more free parameter into the light-curve fitting. On the other hand, it offers the exciting possibility

of deducing the magnetization of stars hosting transiting planets. In particular, the limb-darkening method opens a unique opportunity to obtain an estimate of stellar magnetic fields.

For solar twins (that is, stars with solar fundamental parameters), this can be directly done by comparing observed limb darkening with the values of magnetic limb darkening from Table 1. For stars with different fundamental parameters, one would first need to calculate differences between observed and non-magnetic REFLD limb darkening (available online via the Max Planck Digital Library at <https://doi.org/10.17617/3.NJ56TR>, via the ExoTiC-LD python package⁵² at <https://github.com/Exo-TiC/ExoTiC-LD/> and via the ExoTETHyS python package⁵³ v2.0.10 at <https://github.com/ucl-exoplanets/ExoTETHyS>). Then these differences must be compared with the offsets between magnetic and REFLD limb darkening from Table 1 to determine the magnetization of a star. However, we note that this algorithm assumes that the magnetic field's effect on limb darkening does not depend on stellar fundamental parameters. We expect this to be a reasonable assumption for stars that are not very different from the Sun (that is, for G dwarfs with $-0.1 \leq M/H \leq 0.1$; Methods). In a forthcoming publication, we will extend calculations of the magnetic limb darkening to stars with different fundamental parameters, allowing the magnetic field to be deduced for a broad class of stars with transiting planets. This is especially timely in anticipation of the upcoming PLATO mission, which will observe tens of thousands of bright stars in the lower main sequence⁵⁴.

The effect of a magnetic field on limb darkening strongly depends on the wavelength (Figs. 3 and 4) and, thus, ignoring it might introduce spurious features in the transmission spectra obtained with JWST and eventually with ARIEL²⁶. This underscores the importance of accounting for the magnetic effect on limb darkening in the analysis of transmission spectra.

Methods

Calculations with MURaM and MPS-ATLAS codes

We utilized the 3D radiative MHD code MURaM^{29,37} (which stands for MPS/University of Chicago Radiative MHD) to simulate the solar atmosphere with different degrees of magnetization using the 'box-in-a-star' approach (that is, simulating a small representative volume that encompasses the stellar or solar surface and near-surface layers both below and above the surface⁵⁵). Then we used the MPS-ATLAS code⁵⁶ to synthesize emergent spectra from the MURaM cubes. MPS-ATLAS utilizes a generalized version^{57,58} of the opacity distribution functions approach⁵⁹, where high-resolution ($R = 500,000$) opacity is rebinned to a lower resolution grid ($R \approx 400$ in the visible spectral domain). This allows for a fast spectral synthesis, even when accounting for more than 100 million atomic and molecular transitions⁶⁰. The full list of opacity sources (including continuum opacities) and a detailed description of the MPS-ATLAS code are given in ref. 56. Both the MURaM and MPS-ATLAS codes have been extensively tested and validated by a number of very sensitive observational tests in numerous publications^{15,37,61–63}.

MURaM solves the MHD conservation equation for partially ionized and compressible plasma to model mass, momentum and the energy transport. The transfer of radiative energy is calculated following a multi-group opacity method⁶⁴ using 12 opacity bins⁶³ constructed from the same opacity distribution functions that are used for the spectral synthesis.

The size of the MURaM box in our simulations is 9 Mm \times 9 Mm (512 \times 512 grid points) in the horizontal direction and 5 Mm (500 grid points) in the vertical direction (4 Mm below the optical surface into the convection zone and 1 Mm above it, covering the lower stellar atmosphere and in particular the photosphere). We use the same formulation of the boundary conditions as in ref. 33. It allows for deep recirculating of the field through the presence of a horizontal field in the upflow regions at the lower boundary of the simulation cube^{29,40}. Such a boundary condition results in the generation of a magnetic field at the solar surface whose averaged value does not depend on the

depth of the simulation cube²⁹ and allowed us to explain ubiquitous small-scale horizontal and mixed-polarity magnetic fields that are always present at the solar surface^{65,66}. To cover the range of possible facular magnetic flux densities, we also executed simulations with added initially vertical, unipolar and homogeneous magnetic fields of 100 G, 200 G and 300 G to the set-up we used for simulating quiet regions, including the SSD. The simulations are then allowed to relax and the magnetic field to interact with the convection, finally leading to kilogauss magnetic features in the intergranular lanes, separated by regions (granules) with very weak fields. This approach allows emulating magnetic fields in facular (plage) and network regions, which are thought to be generated by the action of a global dynamo and thus account for their effects on atmospheric structures^{41,45,67}.

We ran our HD and SSD simulations for four solar hours each, while all simulations with an added vertical magnetic field were run for two hours each (after the field has relaxed into a statistically steady state). The MPS-ATLAS code⁵⁶ was then used to calculate spatially averaged spectra emergent from the cubes with 90 second cadence at 10 disk positions, from the disk centre ($\mu = 1.0$) to the limb ($\mu = 0.1$) with a step in μ of 0.1. The intensity emerging from one snapshot of our 100 G simulations is shown in Supplementary Fig. 1 at three wavelengths and for three μ values.

Subsequently, the computed spectra were time-averaged to effectively average out the variability of the spectra caused by granulation and oscillations. Finally, these averaged spectra are used to calculate the limb darkening in the Kepler passband. We have used the time series of our spectra to calculate the error of the mean spectrum in the Kepler passband and have checked that it is well below 0.1% at all disk positions for all the magnetizations considered.

Dependence of the limb darkening on stellar fundamental parameters and magnetic field

The limb darkening strongly depends on stellar fundamental parameters, that is, effective temperature, metallicities and surface gravity^{15,16,68}. REFLD was computed for specific fundamental parameters of stars from the Kepler sample considered. We then perform time-costly 3D radiative MHD simulation runs of magnetic effects only for a star with solar fundamental parameters. In other words, we used REFLD to account for a pretty strong dependence of limb darkening on fundamental parameters¹⁵ and then calculated the magnetic effect using a solar simulation. The latter is a good approximation as stars in the considered Kepler sample have near-solar fundamental parameters.

Magnetic field modifies the limb darkening curve. In Table 1, we present the 3D MURaM limb darkening coefficients derived from the limb darkening with different levels of magnetization in the Kepler passband. The increase of magnetic field makes the limb darkening shallower, that is, brightness near the limb relative to disk centre drops by a small amount. This is reflected in both coefficients: h'_1 increases and h'_2 decreases with increasing magnetic field. The largest drop in intensity from centre to limb is produced by non-magnetic (HD) simulations. In Extended Data Fig. 3a, we show offsets between observed and REFLD limb darkening for stars from our full Kepler sample. This sample consists of stars from ref. 12, where we excluded three most active stars (HAT-P-7, Kepler-17, Kepler-423) with the ratio of in-transit to out-of-transit variability larger than 1.2 (see ref. 12). While a large number of stars cluster along the computed dependence of $\Delta h'_1$ and $\Delta h'_2$ on magnetic field, there are also some outliers. There are two main reasons for these outliers. First, there are observational errors that are averaged out in the comparison presented in Fig. 1. Second, while one can expect that the amplitude of the magnetic effect on the limb darkening depends on stellar fundamental parameters, our calculations are limited to the Sun. In Extended Data Fig. 3b, we separately show the stars with near-central transits (impact parameter $b < 0.5$) so that the planetary trajectory crosses a relatively large part of the stellar disk and therefore extraction of limb darkening is more reliable. From those

Table 2 | Wavelength ranges of some existing or planned photometric (Kepler³⁵, TESS⁷⁰, CHEOPS⁷¹, PLATO⁵⁴) and spectroscopic (JWST/NIRSpec⁴⁷, ARIEL²⁶, ELT/METIS⁷²) instruments

Instrument	Wavelength range (nm)
Kepler	430–890
TESS	600–1,000
CHEOPS	400–1,100
PLATO	500–1,000
JWST/NIRSpec	600–5,300
ARIEL	600–7,800
ELT/METIS	3,000–5,000

stars, we create our selected sample, focusing on stars with near-solar metallicity ($-0.1 \leq M/H \leq 0.1$). These stars show much less scatter around the simulation line.

All in all, Extended Data Fig. 3 hints that the effect of magnetic field on limb darkening strongly depends on metallicity. At the same time, it shows that solar calculations can be used for stars with metallicity values $-0.1 \leq M/H \leq 0.1$.

Test against solar measurements

We compare our calculations of the limb darkening for the quiet solar conditions (SSD case) to spatially resolved narrow-band solar measurements^{42,43} at a number of continuum wavelengths (Fig. 2). These measurements have been processed by the observers to remove any apparent manifestation of magnetic activity. Our model demonstrates an excellent agreement with these observations (within 2% difference around 400 nm and decreasing to less than 1% towards the infrared). This agreement stems partly from the fact that the 3D MURaM calculations include comprehensive calculations of the convection and overshoot⁶³, which allows an accurate reproduction of the limb darkening. In the blue spectral range, it is difficult to find real continuum where the measurements are done, so the errors are larger in this region, but decreasing towards the infrared. In Extended Data Fig. 2, we present the comparison of the solar measurements with the computations with higher magnetic fields (100 G, 200 G and 300 G) at different disk positions. Increasing magnetic field leads to larger difference between observations and computations (Extended Data Fig. 2), leading us to conclude that the best model to reproduce quiet Sun measurements is the SSD model. In particular, our SSD model shows a good performance in the spectral region above 500 nm. This is encouraging as most of the transit photometry and spectroscopy measurements are performed in this spectral domain (Table 2).

Spatial distribution of magnetic field on the solar surface

We present the horizontal distribution of vertical magnetic field in Extended Data Fig. 1 for the same still from which we computed the intensity maps (Supplementary Fig. 1). The magnetic field in the intergranular lanes and in the forming active regions reaches values of up to about 1–2 kilogauss, while for the granules the vertical magnetic field is quite small.

Wavelength range and precision of considered instruments

In Table 2 we present the list of instruments used for detection of planetary transits and for transmission spectroscopy.

Transit light curves

The change of the limb darkening induced by surface magnetic field affects the entire transit profile. In Extended Data Fig. 4, we illustrate this for the exemplary case of the transit of WASP-39 b in front of its host star. The calculations have been performed by approximating

the limb darkening of WASP-39 by that of the Sun (which is reasonable for illustrative purposes as WASP-39 has near-solar fundamental parameters, $T_{\text{eff}} = 5,400 \text{ K} \pm 150 \text{ K}$ and $M/H = -0.12 \pm 0.1$) and using the orbital parameter of WASP-39 b from Table 1 of ref. 14.

The effect of the magnetic field

There are two main mechanisms of the magnetic field by which it impacts the limb darkening. First, a magnetic field leads to the extra heating of the middle and upper photosphere, decreasing the temperature gradient and, thus, making limb darkening less steep. Second, a magnetic field leads to a pronounced corrugation of the optical surface⁶⁹. Closer to the limb, deeper and hotter layers of granular wall are seen, leading to an increase of brightness relative to the non-magnetic case⁶⁹.

In Fig. 1, we assess the relative contribution of these two effects. Namely, we show the effect of magnetic field on horizontally averaged temperature structure in our simulations and compare limb darkening computed from these averaged 1D structures with full calculations. While the 1D calculations account for the extra heating of the photosphere, only the full 3D calculations can catch the corrugation of the optical surface and the effect of hot granular walls. Heating of the photosphere explains approximately 50% of the magnetic effect for $\mu \geq 0.5$. At the same time, it has very little effect on near the limb regions magnetic brightening is driven by the 3D effects.

Data availability

The limb-darkening spectra for the G2 star with different levels of magnetization computed with MURaM and MPS-ATLAS codes are available as Supplementary data.

Code availability

The MPS-ATLAS and MURaM codes used in the current study are available from the corresponding author upon reasonable request.

References

- Schwarzschild, K. On the equilibrium of the Sun's atmosphere. *Nachr. Königl. Ges. Wiss. Göttingen Math. Phys.* **195**, 41–53 (1906).
- Milne, E. A. Radiative equilibrium in the outer layers of a star. *Mon. Not. R. Astron. Soc.* **81**, 361–375 (1921).
- Hestroffer, D. Centre to limb darkening of stars. New model and application to stellar interferometry. *Astron. Astrophys.* **327**, 199–206 (1997).
- Kopal, Z. Detailed effects of limb darkening upon light and velocity curves of close binary systems. *Harv. Coll. Observatory Circular* **454**, 1–12 (1950).
- Lanza, A. F., Rodonò, M., Pagano, I., Barge, P. & Llebaria, A. Modelling the rotational modulation of the Sun as a star. *Astron. Astrophys.* **403**, 1135–1149 (2003).
- Zhao, J., Nagashima, K., Bogart, R. S., Kosovichev, A. G. & Duvall, T. L. Systematic center-to-limb variation in measured helioseismic travel times and its effect on inferences of solar interior meridional flows. *Astrophys. J. Lett.* **749**, L5 (2012).
- Kostogryz, N. M., Fournier, D. & Gizon, L. Modelling continuum intensity perturbations caused by solar acoustic oscillations. *Astron. Astrophys.* **654**, A1 (2021).
- Seager, S. & Sasselov, D. D. Theoretical transmission spectra during extrasolar giant planet transits. *Astrophys. J.* **537**, 916–921 (2000).
- Brown, T. M., Charbonneau, D., Gilliland, R. L., Noyes, R. W. & Burrows, A. Hubble Space Telescope time-series photometry of the transiting planet of HD 209458. *Astrophys. J.* **552**, 699–709 (2001).
- Charbonneau, D., Brown, T. M., Noyes, R. W. & Gilliland, R. L. Detection of an extrasolar planet atmosphere. *Astrophys. J.* **568**, 377–384 (2002).

11. Maxted, P. F. L. Comparison of the power-2 limb-darkening law from the STAGGER-grid to Kepler light curves of transiting exoplanets. *Astron. Astrophys.* **616**, A39 (2018).
12. Maxted, P. F. L. Limb darkening measurements from TESS and Kepler light curves of transiting exoplanets. *Mon. Not. R. Astron. Soc.* **519**, 3723–3735 (2023).
13. Kervella, P., Bigot, L., Gallenne, A. & Thévenin, F. The radii and limb darkening of α Centauri A and B. Interferometric measurements with VLT/PIONIER. *Astron. Astrophys.* **597**, A137 (2017).
14. Rustamkulov, Z. et al. Early Release Science of the exoplanet WASP-39b with JWST NIRSpec PRISM. *Nature* **614**, 659–663 (2023).
15. Kostogryz, N. M. et al. Stellar limb darkening. A new MPS-ATLAS library for Kepler, TESS, CHEOPS, and PLATO passbands. *Astron. Astrophys.* **666**, A60 (2022).
16. Sing, D. K. Stellar limb-darkening coefficients for CoRoT and Kepler. *Astron. Astrophys.* **510**, A21 (2010).
17. Claret, A. & Bloemen, S. Gravity and limb-darkening coefficients for the Kepler, CoRoT, Spitzer, uvby, UBVRIJHK, and Sloan photometric systems. *Astron. Astrophys.* **529**, A75 (2011).
18. Neilson, H. R. & Lester, J. B. Spherically symmetric model stellar atmospheres and limb darkening. II. Limb-darkening laws, gravity-darkening coefficients and angular diameter corrections for FGK dwarf stars. *Astron. Astrophys.* **556**, A86 (2013).
19. Claret, A. A new method to compute limb-darkening coefficients for stellar atmosphere models with spherical symmetry: the space missions TESS, Kepler, CoRoT, and MOST. *Astron. Astrophys.* **618**, A20 (2018).
20. Morello, G. et al. First Release of PLATO Consortium stellar limb-darkening coefficients. *Res. Notes Am. Astron. Soc.* **6**, 248 (2022).
21. Espinoza, N. & Jordán, A. Limb darkening and exoplanets: testing stellar model atmospheres and identifying biases in transit parameters. *Mon. Not. R. Astron. Soc.* **450**, 1879–1899 (2015).
22. Knutson, H. A., Charbonneau, D., Noyes, R. W., Brown, T. M. & Gilliland, R. L. Using stellar limb-darkening to refine the properties of HD 209458b. *Astrophys. J.* **655**, 564–575 (2007).
23. Kreidberg, L. et al. A detection of water in the transmission spectrum of the hot Jupiter WASP-12b and implications for its atmospheric composition. *Astrophys. J.* **814**, 66 (2015).
24. Espinoza, N. & Jordán, A. Limb darkening and exoplanets—II. Choosing the best law for optimal retrieval of transit parameters. *Mon. Not. R. Astron. Soc.* **457**, 3573–3581 (2016).
25. Gardner, J. P. et al. The James Webb Space Telescope. *Space Sci. Rev.* **123**, 485–606 (2006).
26. Tinetti, G. et al. A chemical survey of exoplanets with ARIEL. *Exp. Astron.* **46**, 135–209 (2018).
27. Reiners, A. Observations of cool-star magnetic fields. *Living Rev. Sol. Phys.* **9**, 1 (2012).
28. Charbonneau, P. Where is the solar dynamo?. *J. Phys. Conf. Ser.* **440**, 012014 (2013).
29. Rempel, M. Numerical simulations of quiet sun magnetism: on the contribution from a small-scale dynamo. *Astrophys. J.* **789**, 132 (2014).
30. Trujillo Bueno, J., Shchukina, N. & Asensio Ramos, A. A substantial amount of hidden magnetic energy in the quiet Sun. *Nature* **430**, 326–329 (2004).
31. del Pino Alemán, T., Trujillo Bueno, J., Štěpán, J. & Shchukina, N. A novel investigation of the small-scale magnetic activity of the quiet Sun via the Hanle effect in the Sr I 4607 Å line. *Astrophys. J.* **863**, 164 (2018).
32. Bhatia, T. S. et al. Small-scale dynamo in cool stars. I. Changes in stratification and near-surface convection for main-sequence spectral types. *Astron. Astrophys.* **663**, A166 (2022).
33. Witzke, V. et al. Small-scale dynamo in cool stars. II. The effect of metallicity. *Astron. Astrophys.* **669**, A157 (2023).
34. Rackham, B. V. et al. The effect of stellar contamination on low-resolution transmission spectroscopy: needs identified by NASA's Exoplanet Exploration Program Study Analysis Group 21. *R. Astron. Soc. Tech. Instrum.* **2**, 148–206 (2023).
35. Borucki, W. J. et al. Kepler Planet-Detection Mission: introduction and first results. *Science* **327**, 977 (2010).
36. Kostogryz, N. et al. MPS-ATLAS library of stellar model atmospheres and spectra. *Res. Notes Am. Astron. Soc.* **7**, 39 (2023).
37. Vögler, A. et al. Simulations of magneto-convection in the solar photosphere. Equations, methods, and results of the MURaM code. *Astron. Astrophys.* **429**, 335–351 (2005).
38. Böhm-Vitense, E. Über die wasserstoffkonvektionszone in sternern verschiedener effektivtemperaturen und leuchtkrafte. *Z. Astrophys.* **46**, 108 (1958).
39. Norris, C. M. et al. Spectral variability of photospheric radiation due to faculae—II. Facular contrasts for cool main-sequence stars. *Mon. Not. R. Astron. Soc.* **524**, 1139–1155 (2023).
40. Rempel, M. Small-scale dynamo simulations: magnetic field amplification in exploding granules and the role of deep and shallow recirculation. *Astrophys. J.* **859**, 161 (2018).
41. Witzke, V. et al. Can 1D radiative-equilibrium models of faculae be used for calculating contamination of transmission spectra? *Astrophys. J. Lett.* **941**, L35 (2022).
42. Pierce, A. K., Slaughter, C. D. & Weinberger, D. Solar limb darkening in the interval 7404–24018 Å, II. *Sol. Phys.* **52**, 179–189 (1977).
43. Neckel, H. & Labs, D. Solar limb darkening 1986–1990 (λ 303 to 1099 nm). *Sol. Phys.* **153**, 91–114 (1994).
44. Solanki, S. K., Krivova, N. A. & Haigh, J. D. Solar irradiance variability and climate. *Annu. Rev. Astron. Astrophys.* **51**, 311–351 (2013).
45. Beeck, B., Schüssler, M., Cameron, R. H. & Reiners, A. Three-dimensional simulations of near-surface convection in main-sequence stars. III. The structure of small-scale magnetic flux concentrations. *Astron. Astrophys.* **581**, A42 (2015).
46. Solanki, S. K., Inhester, B. & Schüssler, M. The solar magnetic field. *Rep. Prog. Phys.* **69**, 563–668 (2006).
47. Jakobsen, P. et al. The Near-Infrared Spectrograph (NIRSpec) on the James Webb Space Telescope. I. Overview of the instrument and its capabilities. *Astron. Astrophys.* **661**, A80 (2022).
48. Lim, O. et al. Atmospheric reconnaissance of TRAPPIST-1 b with JWST/NIRISS: evidence for strong stellar contamination in the transmission spectra. *Astrophys. J. Lett.* **955**, L22 (2023).
49. Lustig-Yaeger, J. et al. A JWST transmission spectrum of the nearby Earth-sized exoplanet LHS 475 b. *Nat. Astron.* **7**, 1317–1328 (2023).
50. Espinoza, N. et al. Spectroscopic time-series performance of JWST/NIRSpec from commissioning observations. *Publ. Astron. Soc. Pac.* **135**, 018002 (2023).
51. Bouwman, J. et al. Spectroscopic time series performance of the mid-infrared instrument on the JWST. *Publ. Astron. Soc. Pac.* **135**, 038002 (2023).
52. Grant, D. & Wakeford, H. R. Exo-TiC/ExoTiC-LD: ExoTiC-LD v3.0.0. *Zenodo* <https://doi.org/10.5281/zenodo.7437681> (2022).
53. Morello, G. et al. ExoTETHyS: tools for exoplanetary transits around host stars. *J. Open Source Softw.* **5**, 1834 (2020).
54. Rauer, H. et al. The PLATO 2.0 mission. *Exp. Astron.* **38**, 249–330 (2014).
55. Magic, Z. et al. The stagger-grid: a grid of 3D stellar atmosphere models. I. Methods and general properties. *Astron. Astrophys.* **557**, A26 (2013).
56. Witzke, V. et al. MPS-ATLAS: a fast all-in-one code for synthesising stellar spectra. *Astron. Astrophys.* **653**, A65 (2021).
57. Cernetic, M. et al. Opacity distribution functions for stellar spectra synthesis. *Astron. Astrophys.* **627**, A157 (2019).

58. Anusha, L. S. et al. Radiative transfer with opacity distribution functions: application to narrowband filters. *Astrophys. J. Suppl. Ser.* **255**, 3 (2021).
59. Hubeny, I. & Mihalas, D. *Theory of Stellar Atmospheres* (Princeton Univ. Press, 2014).
60. Kurucz, R. L. ATLAS12, SYNTHÉ, ATLAS9, WIDTH9, et cetera. *Mem. Soc. Astron. Ital. Suppl.* **8**, 14 (2005).
61. Shapiro, A. I. et al. The nature of solar brightness variations. *Nat. Astron.* **1**, 612–616 (2017).
62. Yeo, K. L. et al. Solar irradiance variability is caused by the magnetic activity on the solar surface. *Phys. Rev. Lett.* **119**, 091102 (2017).
63. Witzke, V. et al. Testing MURaM and MPS-ATLAS against the quiet solar spectrum. *Astron. Astrophys.* **681**, A81 (2024).
64. Nordlund, A. Numerical simulations of the solar granulation. I. Basic equations and methods. *Astron. Astrophys.* **107**, 1–10 (1982).
65. Danilovic, S. et al. Transverse component of the magnetic field in the solar photosphere observed by SUNRISE. *Astrophys. J. Lett.* **723**, L149–L153 (2010).
66. Buehler, D., Lagg, A. & Solanki, S. K. Quiet Sun magnetic fields observed by Hinode: support for a local dynamo. *Astron. Astrophys.* **555**, A33 (2013).
67. Salhab, R. G. et al. Simulation of the small-scale magnetism in main-sequence stellar atmospheres. *Astron. Astrophys.* **614**, A78 (2018).
68. Claret, A. A new non-linear limb-darkening law for LTE stellar atmosphere models. Calculations for $-5.0 \leq \log[M/H] \leq +1$, $2000\text{K} \leq T_{\text{eff}} \leq 50000\text{K}$ at several surface gravities. *Astron. Astrophys.* **363**, 1081–1190 (2000).
69. Carlsson, M., Stein, R. F., Nordlund, Å & Scharmer, G. B. Observational manifestations of solar magnetoconvection: center-to-limb variation. *Astrophys. J. Lett.* **610**, L137–L140 (2004).
70. Ricker, G. R. et al. Transiting Exoplanet Survey Satellite (TESS). *J. Astron. Telesc. Instrum. Syst.* **1**, 014003 (2015).
71. Cessa, V. et al. CHEOPS: a space telescope for ultra-high precision photometry of exoplanet transits. In *International Conference on Space Optics – ICSO 2014, Society of Photo-Optical Instrumentation Engineers (SPIE) Conference Series* Vol. 10563 (eds Sodnik, Z. et al.) 105631L (SPIE, 2017).
72. Brandl, B. R. Status of the mid-infrared E-ELT imager and spectrograph METIS. In *Ground-based and Airborne Instrumentation for Astronomy VI, Society of Photo-Optical Instrumentation Engineers (SPIE) Conference Series* Vol. 9908 (eds Evans, C. J. et al.) 990820 (SPIE, 2016).
- Synergy Grant WHOLESUN 810218 and DLR grant PLATO Data Center (DLR FKZ 50OP1902).

Author contributions

N.M.K., A.I.S. and S.K.S. conceived the study. N.M.K., V.W. and A.I.S. conducted the simulations and analysed the results. N.M.K., A.I.S., S.S., S.K.S. and J.V. wrote the paper. R.H.C., L.G., N.A.K., H.-G.L., P.F.L.M., S.S., S.K.S. and J.V. contributed to the analysis of the data. All authors discussed the results and reviewed the paper.

Funding

Open access funding provided by Max Planck Society.

Competing interests

The authors declare no competing interests.

Additional information

Extended data is available for this paper at <https://doi.org/10.1038/s41550-024-02252-5>.

Supplementary information The online version contains supplementary material available at <https://doi.org/10.1038/s41550-024-02252-5>.

Correspondence and requests for materials should be addressed to Nadiia M. Kostogryz.

Peer review information *Nature Astronomy* thanks Andrea Chiavassa and Paul Cristofari for their contribution to the peer review of this work.

Reprints and permissions information is available at www.nature.com/reprints.

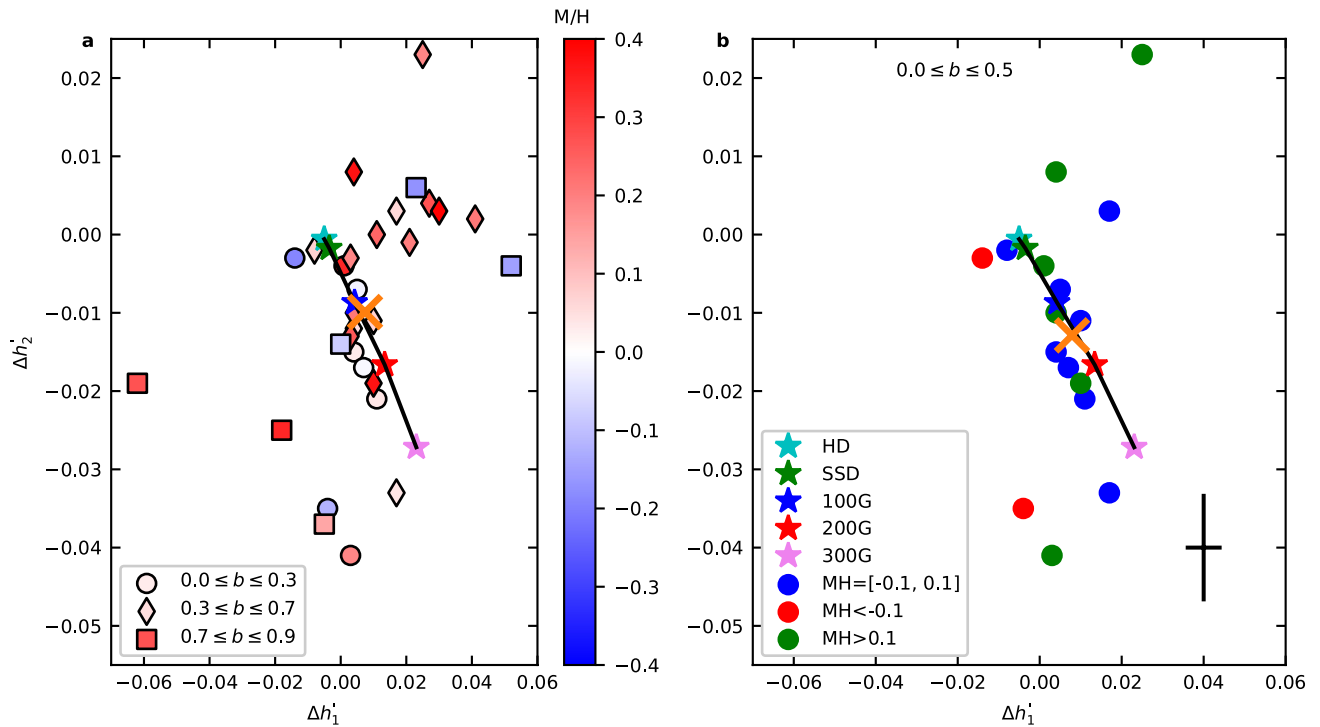
Publisher's note Springer Nature remains neutral with regard to jurisdictional claims in published maps and institutional affiliations.

Open Access This article is licensed under a Creative Commons Attribution 4.0 International License, which permits use, sharing, adaptation, distribution and reproduction in any medium or format, as long as you give appropriate credit to the original author(s) and the source, provide a link to the Creative Commons licence, and indicate if changes were made. The images or other third party material in this article are included in the article's Creative Commons licence, unless indicated otherwise in a credit line to the material. If material is not included in the article's Creative Commons licence and your intended use is not permitted by statutory regulation or exceeds the permitted use, you will need to obtain permission directly from the copyright holder. To view a copy of this licence, visit <http://creativecommons.org/licenses/by/4.0/>.

© The Author(s) 2024

Acknowledgements

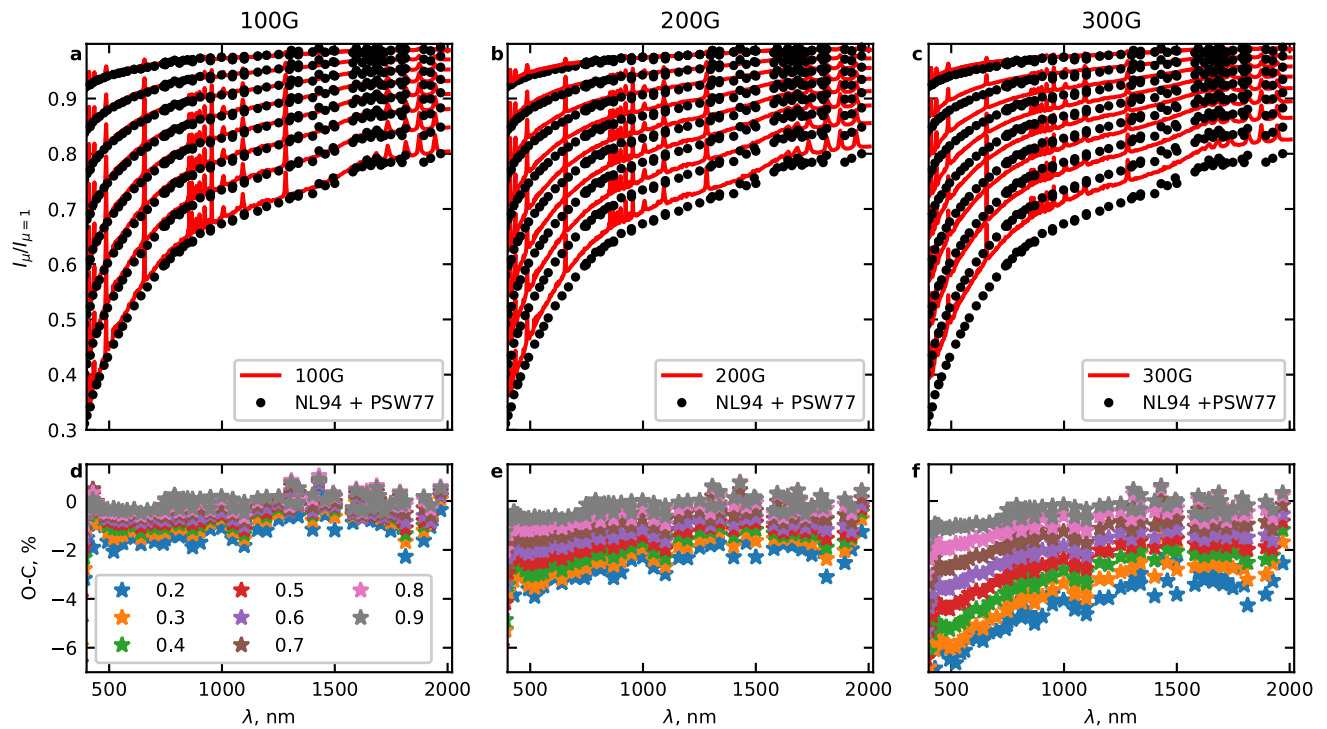
This work has received funding from the European Research Council (ERC) under the European Union's Horizon 2020 research and innovation programme (grant agreement no. 715947). This work has been partially supported from the German Aerospace Center (DLR FKZ 50OP1902). This work was supported in part by ERC



Extended Data Fig. 1 | Limb darkening of individual stars in Kepler passband.

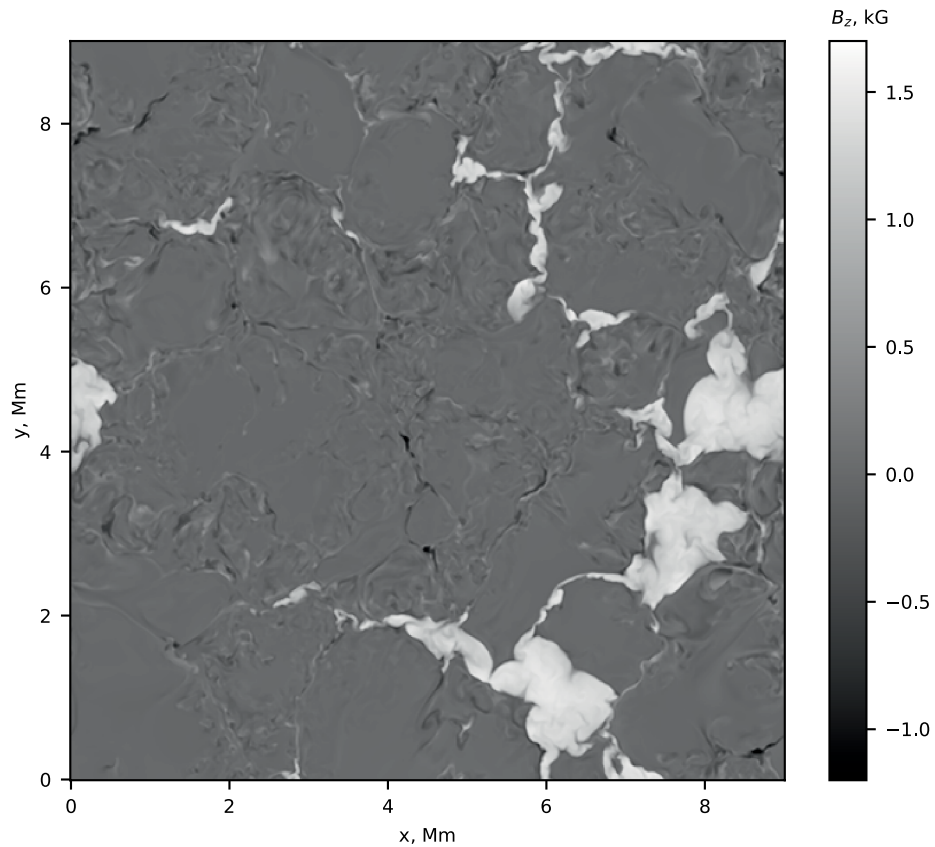
We show the offsets of the limb darkening coefficients for individual stars (Maxted 2023) observed with Kepler. The starred symbols are the same as in kostogryz_figure_1.eps. Panel **a** shows our full sample (see text). The metallicities of the stars are indicated by their colors which refer to the color bar on the right. Different symbols correspond to transits with different impact parameters b . Panel **b** shows only stars with near-central transits ($b < 0.5$). Stars with metallicity values $-0.1 \leq M/H \leq 0.1$ are shown in blue (and referred to as a selected sample,

see text). The stars with higher and lower metallicities are shown in green and red, respectively. The error bars in the right corner of the panel illustrate the root mean square uncertainty of the offsets of shown stars (individual uncertainties are taken from Maxted 2023¹²). The mean values of the offsets are computed for the full and the selected samples and indicated by the orange crosses in panels **a** and **b**, respectively. The selected sample is well described by our solar magnetic simulations.



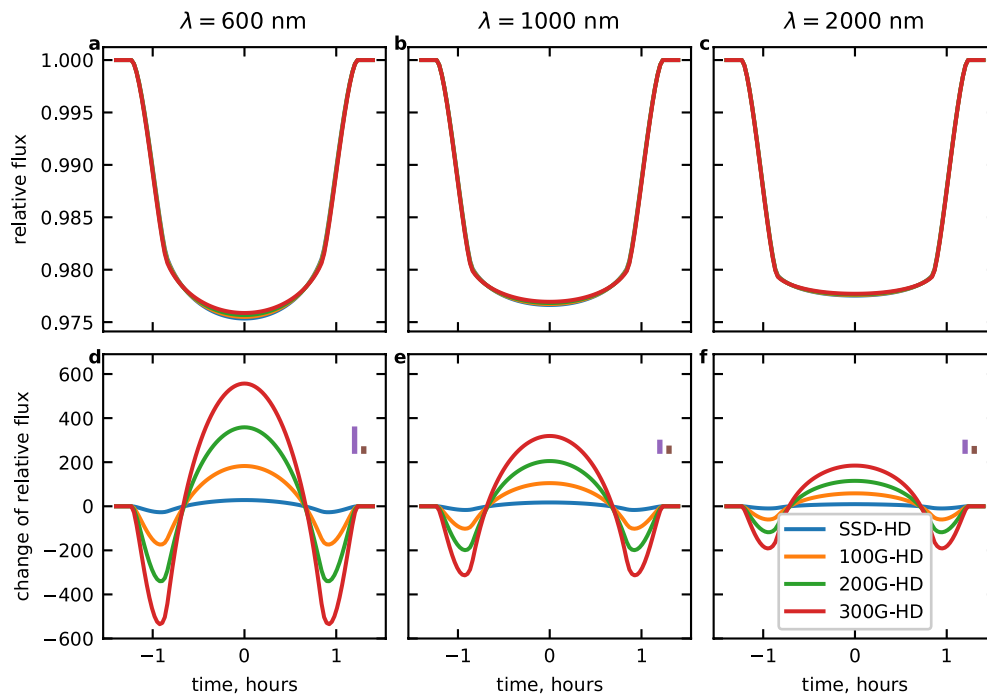
Extended Data Fig. 2 | Magnetized solar limb darkening. We show spectral limb darkening ($I_\mu/I_{\mu=1}$) at different μ (labeled on the left side of the upper row in the figure). Solid lines correspond to our calculations for the different magnetization (different columns correspond to 100G (panels **a** and **d**), 200G (panels **b** and **e**), 300G (panels **c** and **f**) cases) while dots are combined solar measurements (NL94+PSW77), where manifestations of solar magnetic activity

are excluded to the extent possible. The panels **d**, **e**, **f** presents the residuals (asterisk) in percentage between observations and computations (O-C) at different disk positions. The residuals increase with respect to the SSD-case (see Figure *kostogryz_figure_2.eps*) and the difference is larger for the computations with higher magnetic field.



Extended Data Fig. 3 | Distribution of vertical magnetic field at the optical surface in a MURaM cube. Shown is the distribution of vertical magnetic field in the same still as in Figure kostogryz_supplementary_figure_1.eps. The grey scale (see bar on right of figure) depicts the vertical component of the values

of magnetic field. Initially homogeneous magnetic field of 100 G is advected by the convection to intergranular lanes. Comparison with Figure kostogryz_supplementary_figure_1.eps. shows that while small-scale kG field leads to bright features, large concentrations lead to the formation of dark features.



Extended Data Fig. 4 | Simulated WASP-39b transit light curves. The transit light curve at different wavelengths (600 nm, 1000 nm and 2000 nm in panels **a**, **b**, and **c**, respectively), calculated assuming different levels of WASP-39 atmospheric magnetization. Differences to non-magnetic (HD) calculations (panels **d**, **e**, and **f** at the corresponding wavelengths). Shown are small-scale dynamo (SSD; blue curve) simulations representing the minimum possible level of magnetic activity as well as fully relaxed simulations with a superposed

initial vertical magnetic field of 100 G (orange), 200 G (green), and 300 G (red). The error bars shown in the right-hand side of the bottom panels are taken from Rustamkulov et al.¹⁴. The larger error bar is the WASP-39b noise from NIRSPEC PRISM at the wavelength in our panels (at a bin width of about 0.5%). The smaller error bars are for transit curves averaged over 500-nm bins. The takeaway is that the change in stellar limb darkening due to surface magnetic fields is discernible with the JWST precision.